Electric Field Modulation of Spin Accumulation in Nb-doped SrTiO3 with Ni/AlOx Spin Injection Contacts

Das, A.; Jousma, S. T.; Banerjee, T.

Published in:
Spin

DOI:
10.1142/S2010324718400040

Publication date:
2018

Electric field modulation of spin accumulation in Nb doped $SrTiO_3$ with Ni/AlO_x spin injection contacts

A. Das,[1] S. T. Jousma,[1] and T. Banerjee[1,*]

[1] *Zernike Institute for Advanced Materials, University of Groningen, Nijenborgh 4, 9747 AG Groningen, The Netherlands*

We demonstrate an electric field control of spin lifetime at room temperature, across a semiconducting interface of Nb:STO using Ni/AlO_x as spin injection contacts. We achieve this by a careful tailoring of the potential landscape in Nb:STO, driven by the strong response of the intrinsically large dielectric permittivity in STO to electric fields. The built-in electric field at the Schottky interface with Nb:STO tunes the intrinsic Rashba spin orbit fields leading to a bias dependence of the spin lifetime in Nb:STO. Such an electric field driven modulation of spin accumulation has not been reported earlier using conventional semiconductors. This not only underpins the necessity of a careful design of the spin injection contacts but also establishes the importance of Nb:STO as a rich platform for exploring spin orbit driven phenomena in complex oxide based spintronic devices.

Keywords: Complex Oxides, semiconductor spintronics, spin accumulation, spin lifetime, Rashba spin-orbit coupling, electric field

The basic building blocks in semiconductor spintronics are associated with the creation, manipulation and detection of spins in a semiconducting channel. These have been widely studied in conventional semiconductors such as Si, Ge, GaAs both by optical as well as electrical means[1–5]. An important advance in semiconductor spintronics, however, will be the possibility to control spin manipulation across the semiconducting channel by electric fields. This has remained elusive in conventional semiconductors but recently demonstrated in an electronically rich semiconductor of doped $SrTiO_3$[6].

$SrTiO_3$ (STO) is an insulator with a band gap of 3.2 eV with conduction band dominated by d-orbitals derived from Ti. STO has a large dielectric permittivity (ϵ_r) at room temperature (~ 300) that increases non-linearly with decreasing temperature by atleast 3 orders of magnitude at 4 K[7,8]. Doping Nb^{5+} at the Ti^{4+} site results in an n-type semiconductor, Nb-doped $SrTiO_3$ (Nb:STO), with unconventional charge transport characteristics[9–11]. The electric field modulation of ϵ_r in semiconducting Nb:STO provides an useful knob to tune charge transport when a metal is interfaced with it[12–14]. Bulk STO is reported to have a large value of spin-orbit coupling (SOC), typically around 10 meV[8,15,16]. The breaking of the inversion symmetry at the surface of STO results in a Rashba spin-orbit coupling that can be tuned with electric field[17] when spin injection contacts such as ferromagnet/tunnel barrier are deposited on it[6]. All these properties make the Nb:STO interface an unique platform to study electric field control of spin accumulation across its interface. Using a three terminal (3T) geometry scheme, we study electric field effects on spin transport across an interface between spin injection contacts of Ni/AlO_x on Nb:STO semiconductor.

For this, spin injection contacts of Ni/AlO_x are engineered at the interface of Nb:STO. This is achieved by depositing a thin tunnel barrier of AlO_x (7 $\AA$) on a low doped Nb:STO (0.1 wt% Nb) resulting in a composite barrier at the interface that comprises of both a tunnelling barrier as well as a Schottky barrier. The thickness of the tunnel barrier is chosen such that an application of a bias results in a large potential drop across the Schottky interface with Nb:STO. Whereas, a Schottky barrier is normally considered to be detrimental for spin transport studies, in our case we exploit the built in electric field at such Schottky interfaces to tune the intrinsic Rashba SOC at the Nb:STO interface leading to an electric field control of the spin lifetime. We observe a variation of the spin lifetime from 36 ps to 80 ps at room temperature for an applied bias varying from -0.5 V to +1 V. A wider tunability of the spin lifetime can be realized by optimizing the thickness of the tunneling barrier and a proper choice of the dopant density in Nb:STO.

I. DEVICE GEOMETRY AND MEASUREMENT DETAILS

Spin injection contacts were fabricated on Nb:STO semiconductors with a doping concentration of 0.01 wt% of Nb. Single crystalline semiconducting substrates for this work were obtained from Crystec GmbH. The as received substrates have mixed surface terminations, i.e. the surface consists of both SrO and TiO_2 sublattices. In order to achieve singly terminated surfaces of TiO_2, the single crystals are chemically treated using a standard protocol. TiO_2 termination is preferred over SrO due to its chemical stability. The Nb:STO substrates are treated with deionized (DI) water for the hydration of SrO that is finally removed by dissolving in buffered hydrofluoric acid (BHF)[18]. Atomic force microscopy (AFM) scans on the surface of Nb:STO, post surface termination shows a stepped TiO_2 surface with a root mean square (RMS) roughness less than 3-4 $\AA$. Soon after the chemical treatment, the substrate is inserted into the load-lock of an electron beam evaporator that is pumped down to a base pressure of 7 x 10^{-7} Torr. The spin injection contacts are

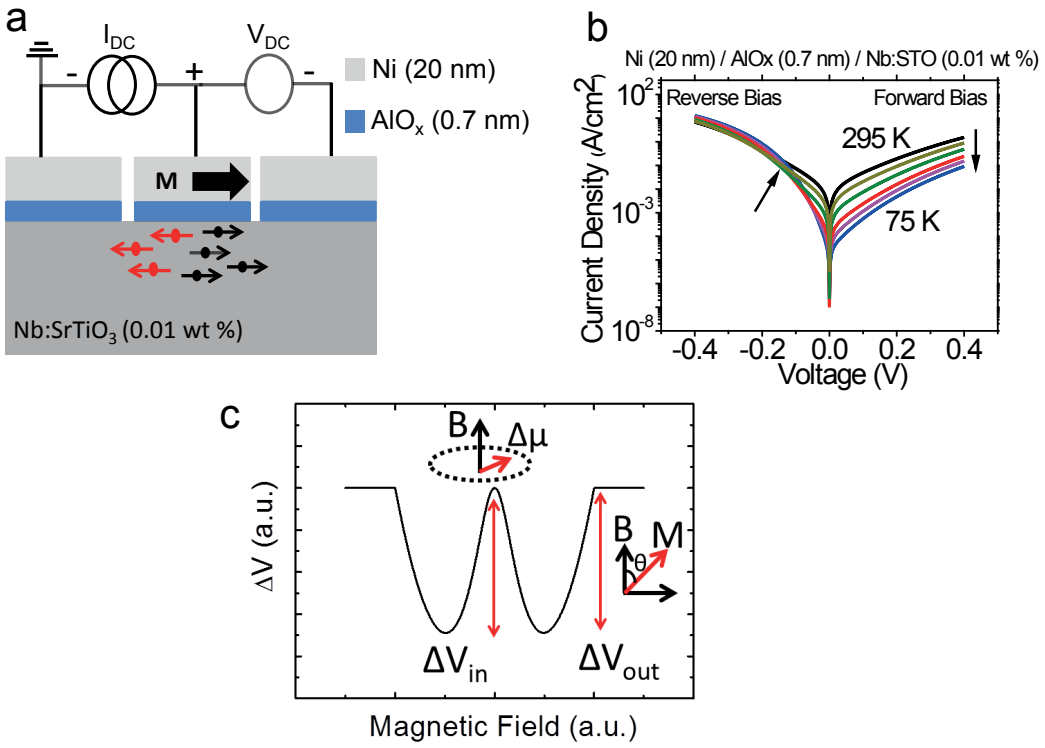

FIG. 1. (a) Electrical measurement scheme using a three terminal (3T) geometry with Ni (20 nm)/AlOx (7Å) spin injection contacts on Nb:STO (0.01 wt% Nb). A constant current (I_{DC}) is sourced across the central spin contact resulting in a non-equilibrium spin accumulation in Nb:STO that is probed by a voltage (V_{DC}) across the same contact. (b) Temperature dependent charge transport characteristics (I-V) across Ni/AlO_x/Nb:STO interface using 3T geometry. Temperature dependence is shown from 295 K (black) to 75 K (blue) with I-V taken at different temperatures such as 250 K, 200 K, 150 K, 120 K, 90 K. The arrow at the forward bias shows the reduction in the forward current whereas at reverse bias it shows an increase in the reverse current with decreasing temperatures. (c) 3T spin voltage response (ΔV) with an oop magnetic field where ΔV_{in} and ΔV_{out} measures the in and out-of-plane spin voltages.

deposited using electron beam evaporation, first a thin layer of Al (7Å) is deposited at a rate of 1 Å/s, followed by an in situ plasma oxidation and subsequent deposition of Ni(20nm)/Au (20nm) with a similar deposition rate. This heterostucture is then patterned into 3T spin injection contact pillars with junction areas ranging from 50 to 200x200 μm^2 using UV lithography and ion beam etching as shown in Fig. 1a.

To study the electrical characteristics of the spin injection contacts, temperature dependent charge transport (I-V) measurements in a 3T geometry were performed. Fig. 1b shows the I-V characteristics at different temperatures. I-V measurements were performed with voltage bias ranging from -0.4 V to +0.4 V. In the forward bias regime, a reduction of the current density with decreasing temperature is observed that indicates thermal activation of the charge carriers across the Schottky interface. On the other hand, an increase in the current density with decreasing temperature is observed at reverse bias conditions indicating increased tunneling across the Nb:STO interface. Due to a large ϵ_r in STO, the conduction bands bend sharply with increasing reverse bias allowing for enhanced tunneling of electrons across the semiconducting interface and leading to unconventional charge transport characteristics across such interfaces[11]. The I-V characteristics are analyzed using the Richardson equation and the Schottky barrier height (SBH) extracted is 0.5 eV (Section IV). The tunneling parameter E_{00} is obtained to be 32 meV ($\sim k_BT$) which is clearly in the regime of thermally assisted field emission (TFE).

For spin injection experiments, a dc current (I_{DC}) is sourced across the central contact that consists of thin Ni films with an in-plane magnetization and a tunnel barrier of AlO_x. The spin polarized carriers from Ni is transferred to the semiconducting Nb:STO via the thin tunneling barrier of AlO_x. This creates a non-equilibrium spin accumulation ($\Delta\mu$) at the semiconducting interface underneath the central contact. The spin accumulation is measured as a spin voltage (ΔV) using voltage probe (V_{DC}) across the same central contact. The voltage probe measures both the charge and spin contribution at the interface of Nb:STO. Thus, ΔV for each bias is extracted by subtracting the charge related background V_{bg} from V_{DC}.

Fig. 1c is a simulation of the expected spin voltage signal when the magnetic field is applied out-of-plane (oop)

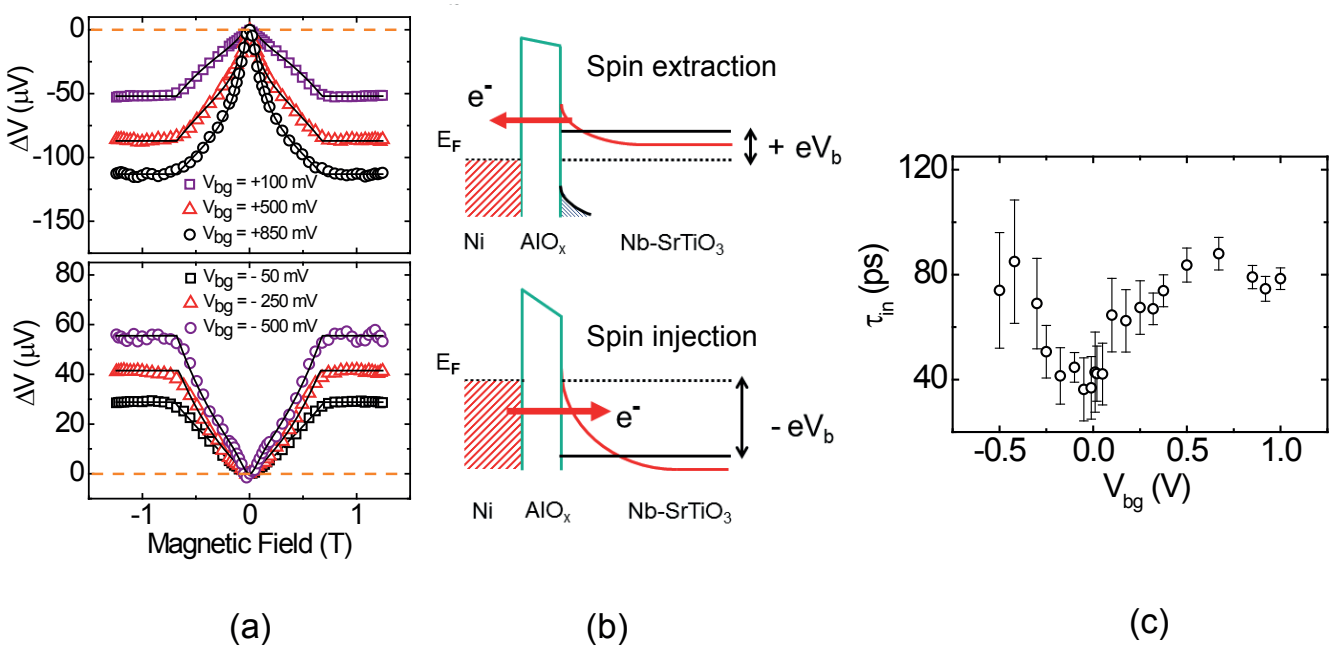

FIG. 2. (a) Left top panel shows the room temperature spin voltage (V) signal with magnetic field applied out-of-plane at different forward bias with the background voltage subtracted at zero voltage shown by the dashed line. The square symbols represent the spin voltage signal at a background voltage (V_{bg}) of +100 mV, triangle for +500mV and circle for +850 mV. The left bottom panel shows the room temperature spin voltage signals at different reverse bias where the background voltage is subtracted similarly at zero voltage shown by the dashed line. The square, triangle and square symbols are for a background voltage of -50 mV, -250mV and -500 mV, respectively. The solid line represents the fit to these curves using Eq. (1). (b) The corresponding change in the potential landscape at the interface for forward bias is shown in the schematic at the top panel. The corresponding potential landscape due to reverse bias is shown in the bottom panel. (c) Variation of $\tau_{\rm in}$ at room temperature with bias V_{bg} obtained by fitting the spin voltage signals with Eq. (1)

to the magnetization of Ni. As a result, the spin accumulation $\Delta\mu$, starts to precess around the magnetic field with a Larmor frequency ω_L, causing spin dephasing in the in-plane direction resulting in a decrease in $\Delta\mu$ and spin voltage signal with a Lorentzian lineshape[19,20]. This is called the Hanle effect. On increasing the magnetic field strength further, the magnetization of Ni starts to rotate and follow the field resulting in a regain of the spin accumulation in oop direction. This increases the spin voltage signal until the saturation magnetization (M_s) of Ni is reached around 650 - 700 mT, as shown by the flat line. The equation that is used to describe this phenomena is the 1D Bloch equation and given by[6] :

$$\Delta V = \Delta V_{out}\cos^2\theta + \frac{\Delta V_{in}\sin^2\theta}{\sqrt{2}}\sqrt{\frac{1+\sqrt{1+(\omega_L\tau_{in})^2}}{1+(\omega_L\tau_{in})^2}} \quad (1)$$

where, ω_L is the Larmor frequency, $\Delta V_{\rm in}$ is the in-plane spin voltage due to spin dephasing, and is a measure of the amplitude of the Lorentzian signal. $\Delta V_{\rm out}$ is the oop spin voltage due to the rotation of the magnetization of Ni with an angle θ with the magnetic field. $\tau_{\rm in}$ is the in-plane spin lifetime that is inversely proportional to the Lorentzian linewidth. The spin voltage signal ΔV is related to the spin accumulation $\Delta\mu$, by $\Delta V = P^2\Delta\mu$, where P is the tunnel spin polarization across the Ni/AlO_x interface.

II. RESULTS AND DISCUSSION

Fig. 2a shows the room temperature spin voltage responses with oop magnetic field by sourcing the current in the forward and reverse bias regime. At forward bias, the spins are extracted at the ferromagnetic interface due to the transport of the electrons from Nb:STO to Ni as shown in Fig. 2b (top panel). This is referred as spin extraction. The top panel of Fig. 2a shows the spin extraction signals at different V_{bg}. The bottom panel, shows the signals at different V_{bg} but in reverse bias regime. This is referred to as spin injection. The dotted line around the zero voltage shows the point where the background signal V_{bg} is subtracted. We observe a change in the magnitude of the spin voltage response with bias at both forward and reverse bias. The responses at forward bias shows a stronger scaling of the spin signals compared to that at reverse bias. The features in the observed signals are different from the simulated signal as shown in Fig. 1c. The signals in Fig. 2a decay with magnetic field in a Lorentzian lineshape followed by an additional broadening that finally saturates around 650-700 mT, corresponding

to the saturation field in Ni. An interesting feature is the disappearance of the ΔV_{out} at all biases. This indicates the presence of an anisotropic spin signal that is comparable to ΔV_{out}. In 3T spin injection studies, there are reports on the presence of the spin signals related to tunneling anisotropic magnetoresistance (TAMR)[21,22]. We believe that we do have spin signals related to TAMR in our devices and their magnitude is quite comparable to that of ΔV_{out} spin signals. The solid blue line is a fit using Eq.1. The values of the parameters concerning the spin dephasing effect i.e. ΔV_{in} and τ_{in} can be extracted from the fit at different V_{bg} but ΔV_{out} cannot be independently extracted due to the strong coupling with TAMR signals.

Fig. 2b shows the potential landscape of the conduction band of STO due to an applied bias both in forward and reverse direction. On increasing the forward bias, the conduction band gradually flattens decreasing the depletion region at the Nb:STO interface. At reverse bias due to large ϵ_r, sharp bending of the conduction band of STO results in an increased tunneling transport that further increases with increasing reverse bias. This not only only leads to unconventional charge transport characteristics as shown in Fig. 1b but also influences spin transport as will be discussed later.

One of the prerequisites for spin injection into a semiconducting channel is direct tunneling transport of the spin polarized carriers from the ferromagnet via the tunnel barrier[23]. This can be impeded due to the presence of the Schottky barrier across a ferromagnet/semiconductor interface. However, we show that a careful engineering of the interface in our devices not only results in the observation of a spin voltage but also its control by the applied bias, V_{bg}. We achieve this control by exploiting the built in electric field at such Schottky barriers and thus effectively tune the spin transport parameters in the semiconducting channel. The in-plane spin lifetime (τ_{in}) is plotted with respect to the junction voltage (V_{bg}) for the bias ranging from -0.5 V to +1 V. Fig. 2c shows the variation of the spin lifetime at room temperature with bias where a continuous increase in the spin lifetime from 36 ps to 80 ps is observed at the forward bias from +0.01 V to +0.5 V, and then saturates. The spin lifetime at the reverse bias on the other hand, increases around the same value but with larger fluctuations of about 12-15%.

At any particular bias V_{bg}, the tunneling of the spin polarized carriers occurs via two barriers, the tunneling barrier of AlO_x and across the depletion region at the STO interface. The latter can be strongly modified due to the unconventional electronic properties in Nb:STO. Due to the large value of ϵ_r in STO at room temperature ($\sim$ 300) and its non-linear dependence on the electric field, there is a strong variation of the conduction band potential with V_{bg} at the Nb:STO interface. This is shown in Fig. 3a, where the built-in electric field decreases by 0.025 V/nm with bias increasing from -0.5 V to +1 V. This change in the built-in electric field with the applied bias is calculated incorporating the variation of ϵ_r of STO in the presence of the tunnel barrier AlO_x[14]. For the electrostatic modelling discussed in Fig. 3a, the flat band condition is fixed at +1.1 V considering the work function of Ni to be 5 eV and electron affinity of Nb:STO as 3.9 eV.

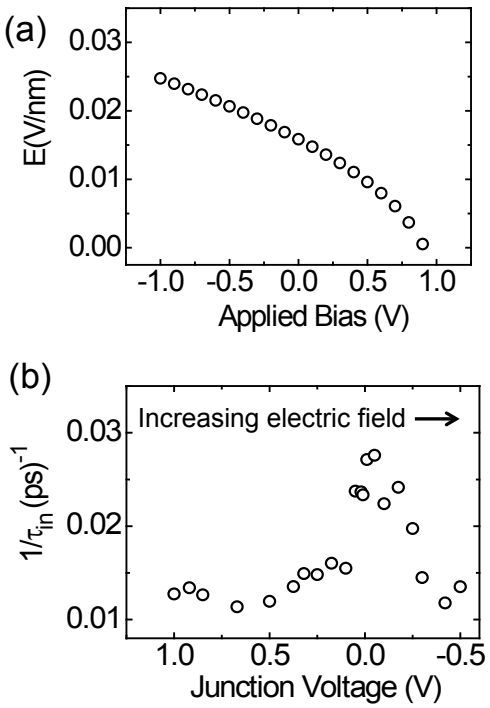

FIG. 3. (a) Variation of the built-in electric field with an applied Schottky bias. The electric field changes by about 0.025 V/nm upto 1 V. At +1.1 V flat band condition is reached (from the Schottky model). (b) Variation of $1/\tau$ with increasing electric field for applied bias (V_{bg}) varying from +1 V to -0.5 V. $1/\tau \sim J_{sf}$ which is the spin flip current due to SOC.

We now discuss the observed saturation in the values of τ_{in} above +0.5 V at the forward bias regime in Fig. 2c. A gradual flattening of the conduction bands in Nb:STO with increasing applied bias (Fig. 2b), decreases the built-in electric field as shown in Fig. 3a. This decreases the tunability of the Rashba SOC and leads to a gradual saturation of τ_{in} at higher forward bias ($\geq$ +0.5 V). Such a bias dependence of the spin lifetime has not been reported in conventional semiconductors. In an earlier report, Han et al. reported on a temperature dependence of the spin lifetime in Nb:STO using CoFe/MgO as spin injection contacts. The spin lifetime of 100 ps at 10 K was found to depend weakly on the applied bias[24]. This can be understood both by the choice of a thick tunnel barrier of MgO (2 nm) and a highly doped Nb:STO (0.7 wt% Nb doping), that does not enable the electric field manipulation of the spin lifetimes. On the other hand, Kamerbeek et al. showed a clear variation of the spin lifetime from 2 to 17 ps with an applied bias, while using

a 0.1 wt% doped Nb:STO and a thin tunnel barrier of 1.1 nm AlO_x and Co as spin injection contacts, at room temperature[6]. This underpins the necessity of carefully tailoring the Schottky interface to attain the desired electric field control of the Rashba spin orbit coupling for spin manipulation in Nb:STO.

We show the variation of $1/\tau_{\rm in}$ with applied bias in Fig. 3b. As discussed in Ref. 6, $1/\tau_{\rm in}$ is proportional to the normalized spin-flip current J_{sf} along the semiconducting interface and its variation with Rashba coupling constant depends on the strength of the potential barrier characterized by the height and width of the barrier. We observe the spin lifetime to vary from 36 to 80 ps at room temperature ($1/\tau_{\rm in}$ varies from 0.01 to 0.025 ps^{-1}). This modest variation signifies the presence of a larger barrier height and width as compared to Ref. 6.

III. SUMMARY

In conclusion, we have demonstrated an electric field control of spin transport across the Nb:STO interface using Ni/AlO_x spin injection contacts at room temperature. We achieve this by exploiting the electric field at the dominant Schottky barrier to tune the intrinsic Rashba SOC across the semiconducting interface of Nb:STO. This cannot be realized in conventional semiconductors and establishes Nb:STO as a rich platform for the exploration of spin orbit coupling driven phenomena in spintronic devices with complex oxides.

The authors would like to thank R. Hamming-Green, H. Vuijk , A. M. Kamerbeek for helpful discussions and J. G. Holstein and H. M. de Roosz for technical support. This work is supported by the Dieptestrategie grant 2014 from the Zernike Institute for Advanced Materials, University of Groningen.

IV. ADDITIONAL INFORMATION

A. Analysis of the charge transport characteristics

The charge transport mechanism is characterized using the temperature dependence of the I-V characteristics. Fig. 4a shows the plot of current density (J) with respect to an applied voltage bias for temperatures ranging from 75 K to RT (295 K). The current densities are plotted at a low voltage bias ranging from -0.4 V to +0.4 V. A reduction in the forward current and an increase in reverse current on reducing temperature is observed (as indicated in the main text in Fig. 1b). As mentioned in the text, increase in the reverse current indicates tunneling of electrons across the Nb:STO interface. This is possible due to the insertion of the oxide tunnel barrier that reduces the Schottky barrier height such that the energy of tunneling E_{00} is almost comparable to k_BT. This is analyzed using the Richardson plot where the saturation current density J_s is obtained by fitting the forward bias current densities at all temperatures (shown in Fig. 4b) using the equation :

$$J = J_s exp(\frac{eV}{nk_BT} - 1) \quad (2)$$

The obtained values of J_s is then used in the equation of thermally assisted field emission (TFE) model to extract the Schottky barrier height (ϕ_B). The equation used to fit the data as shown in Fig. 4c by the dashed plot is given by[12]:

$$\frac{J_s}{T^2} = \frac{AE_{00}^{1/2}(e\phi_B - \xi)exp(-\frac{\xi}{k_BT} - \frac{e\phi_B - \xi}{E})}{k_BTcosh\frac{E_{00}}{k_BT}} \quad (3)$$

where $E = E_{00}coth\frac{E_{00}}{k_BT}$, A is the Richardson constant which is 156 $Acm^{-2}K^{-2}$ for Nb:STO and ξ is the degeneracy. By fitting the equation in Fig. 4c where J_s/T^2 is plotted with respect to 1000/T, the Schottky barrier height ϕ_B is obtained as 0.5 eV, E_{00} as 32 meV and ξ as -20 meV.

E_{00} is comparable to k_BT at room temperature indicating a transport mechanism that has both thermionic and tunneling characteristics and agrees with the I-V plots we obtained (shown in Fig. 4a). The potential profile across the interface of Nb:STO at zero bias is shown in Fig. 4d. The insertion of a 7$\AA$ thick tunnel barrier reduces ϕ_B from that predicted by Schottky-Mott model (1.05 eV for a Schottky interface of Ni with Nb:STO). Interestingly, the degeneracy is negative for this doping concentration of Nb:STO whereas in the earlier reports[13], the degeneracy is reported to be positive (i.e. a non-degenerate semiconductor). The depletion region is calculated to be 70 nm using the equation $W_d = \sqrt{\frac{2\epsilon_r\phi_B}{eN_D}}$, where ϵ_r is 300 and N_D is 3x10^{18} cm^{-3} when measured earlier for Nb:STO (0.01 wt%) substrates using Van der Pauw measurements[10].

B. Origin of an additional MR at a magnetic field greater than saturation magnetization of Ni

In addition to the observation of spin injection (Lorentzian MR) and TAMR signals (parabolic MR), another parabolic MR is observed at a magnetic field greater than the saturation magnetization of Ni, i.e beyond $\pm 0.65T$. Not much is known about the origin of such an additional MR. Assuming this MR to originate from the semiconductor, it is subtracted from the background by fitting a parabola at $B > \pm 0.65$ T. Fig. 5a shows the spin signals as shown in Fig. 2a, but without subtracting the background parabolic MR for both forward (+ V_{bg}) and reverse bias (- V_{bg}) respectively. It is fitted with the same eq.1 but with a constant function at $B > \pm 0.65$ T. As is shown in Fig. 5b the difference in the

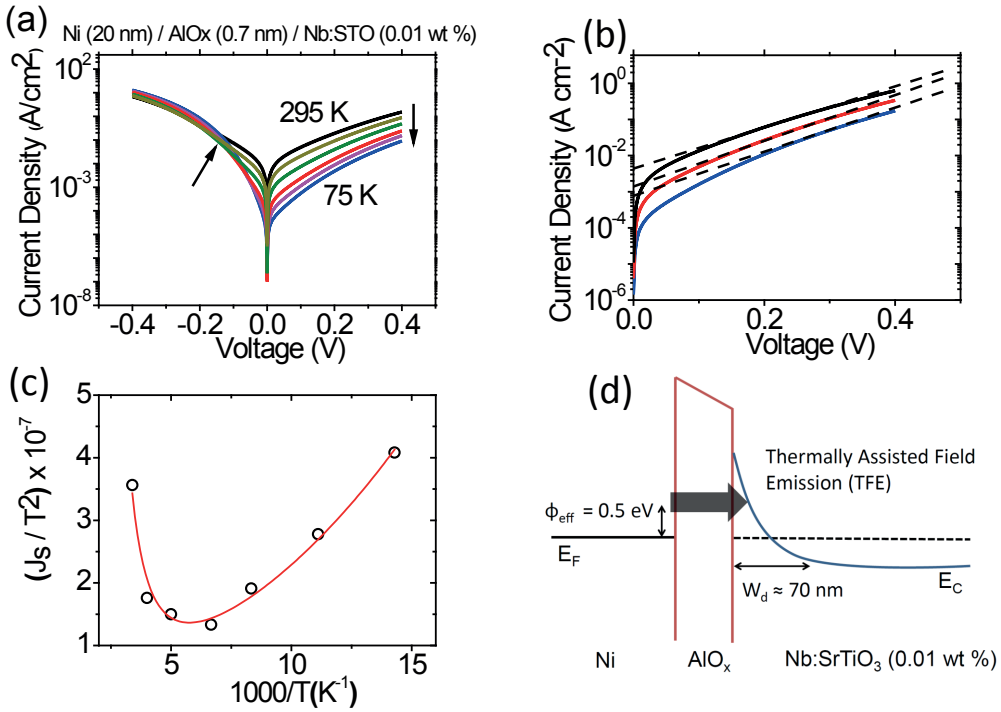

FIG. 4. (a) Temperature dependent I-V characteristics where current density J is plotted with respect to voltage bias for a bias range of -0.4 to +0.4 V for the device Ni (20 nm)/ AlO_x (7Å) / Nb:STO (0.01 wt%). (b) Saturation current density (J_s) is extracted from a fit to the forward bias characteristics at different temperatures using Eq. 2 as shown by the solid line. (c) J_s/T^2 plotted with 1000/T and the variation is fitted using Eq. 3, indicating TFE transport. (d) From the fit to Eq. 3, Schottky barrier height (ϕ_B) is extracted that shows the reduction from the value predicted from the Schottky-Mott model. The potential profile at zero bias shows a degeneracy in the semiconductor as shown by ξ with a large depletion region shown by W_d.

residual due to the fitting without subtracting the background MR causes an increasing trend in the residual plot that indicates the presence of a weak MR signal beyond the saturation value of Ni as shown by the black symbols whereas red symbols indicates a constant noise around 0 μV indicating a subtracted parabolic background MR. This subtraction of the background MR changes the values of ΔV_{in}, ΔV_{out}, τ_{in} but not significantly. However, the overall trend with respect to the junction voltage was not altered.

C. Inverted Hanle signals

Presence of magnetostatic stray fields at the ferromagnetic interface reduces the spin accumulation as has been reported[25]. This can be observed by applying a magnetic field in-plane to the interface resulting in an Lorentzian lineshape that is inverted in sign to the conventional Hanle effect. This is called the inverted Hanle effect. This is reported to alter the spin accumulation signals by causing an additional broadening of the Lorentzian lineshape of Hanle signal and decreasing the spin lifetime[25].

Fig. 6a shows the inverted Hanle signals with increasing forward bias (+ V_{bg}). It shows an inverted Lorentzian shape but the magnitude of the signal is very weak compared to the Hanle signals. It has been reported in earlier works that the magnetostatic stray field increases with increasing saturation magnetization of the ferromagnet. In our case, we have used a soft ferromagnet, Ni and the surface roughness of the heterostructure post growth was less than 6 Å. This explains the weaker contribution of the stray fields on the inverted Hanle signals. This weak variation with bias is also observed at reverse bias where the signal to noise ratio is very low and Lorentzian signals are hard to distinguish as shown in Fig. 6b.

* corresponding author; t.banerjee@rug.nl

[1] B. T. Jonker, G. Kioseoglou, A. T. Hanbicki, C. H. Li, and P. E. Thompson, Nature Physics **3**, 542 (2007).

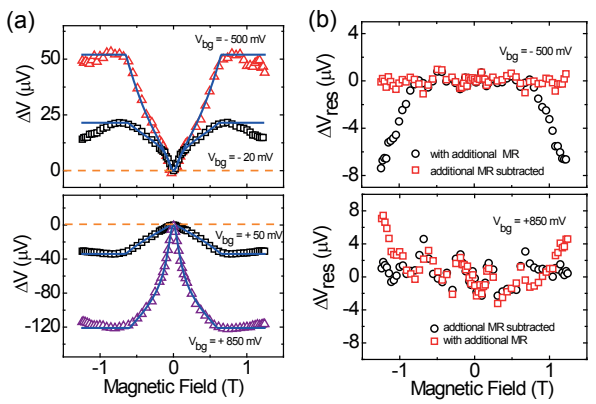

FIG. 5. (a) Spin signals at different forward and reverse bias at room temperature. The presence of an additional MR is observed at $B > \pm 0.65$ T. Beyond this value a good fitting of the data is not possible. (b) This fitting results in an increasing value of the residual signal at around $B > \pm 0.65$ T which is indicated by black symbols both for forward and reverse bias. The red symbols show the residuals after subtracting the additional background and fitting with Eq.1.

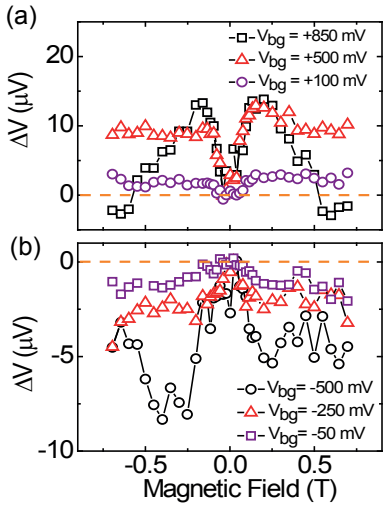

FIG. 6. (a) Inverted Hanle signals at different $+V_{bg}$ is plotted with applied magnetic field in-plane at room temperatures. The spin signals shows a weak bias dependence and are significantly small compared to the Hanle signals. The charge background signals are subtracted at the zero voltage which is shown by the dashed line. (b) Inverted Hanle signals for negative V_{bg}s showing a low signal to noise ratio.

[2] X. Lou, C. Adelmann, S. A. Crooker, E. S. Garlid, J. Zhang, K. S. M. Reddy, S. D. Flexner, C. J. Palmstrøm, and P. A. Crowell, Nature Physics **3**, 197 (2007).

[3] S. P. Dash, S. Sharma, R. S. Patel, M. P. De Jong, and R. Jansen, Nature **462**, 491 (2009).

[4] M. Tran, H. Jaffrès, C. Deranlot, J. M. George, A. Fert, A. Miard, and A. Lemaître, Physical Review Letters **102**, 036601 (2009).

[5] K. Hamaya, Y. Baba, G. Takemoto, K. Kasahara, S. Yamada, K. Sawano, and M. Miyao, Journal of Applied Physics **113**, 183713 (2013).

[6] A. M. Kamerbeek, P. Högl, J. Fabian, and T. Banerjee, Physical Review Letters **115**, 136601 (2015).

[7] R. C. Neville, B. Hoeneisen, and C. A. Mead, Journal of Applied Physics **43**, 2124 (1972).

[8] J. A. Sulpizio, S. Ilani, P. Irvin, and J. Levy, Annual Review of Materials Research **44**, 117 (2014).

[9] A. Spinelli, M. A. Torija, C. Liu, C. Jan, and C. Leighton, Physical Review B **81**, 155110 (2010).

[10] K. G. Rana, V. Khikhlovskyi, and T. Banerjee, Applied Physics Letters **100**, 213502 (2012).

[11] A. M. Kamerbeek, E. K. De Vries, A. Dankert, S. P. Dash, B. J. Van Wees, and T. Banerjee, Applied Physics Letters **104**, 212106 (2014).

[12] H. Hasegawa and T. Nishino, Journal of Applied Physics **69**, 1501 (1991).

[13] S. Suzuki, T. Yamamoto, H. Suzuki, K. Kawaguchi, K. Takahashi, and Y. Yoshisato, Journal of Applied Physics **81**, 6830 (1997).

[14] A. M. Kamerbeek, T. Banerjee, and R. J. Hueting, Journal of Applied Physics **118**, 225704 (2015).

[15] G. Khalsa, B. Lee, and A. H. Macdonald, Physical Review B - Condensed Matter and Materials Physics **88**, 041302 (2013).

[16] H. Nakamura, T. Koga, and T. Kimura, Physical Review Letters **108**, 206601 (2012).

[17] A. D. Caviglia, M. Gabay, S. Gariglio, N. Reyren, C. Cancellieri, and J. M. Triscone, Physical Review Letters **104**, 126803 (2010).

[18] G. Koster, B. L. Kropman, G. J. H. M. Rijnders, D. H. A. Blank, and H. Rogalla, Applied Physics Letters **73**, 2920 (1998).

[19] I. Žutić, J. Fabian, and S. D. Sarma, Reviews of Modern Physics **76**, 323 (2004).

[20] F. J. Jedema, H. B. Heersche, A. T. Filip, J. J. A. Baselmans, and B. J. Van Wees, Nature **416**, 713 (2002).

[21] S. Sharma, A. Spiesser, H. Saito, S. Yuasa, B. J. Van Wees, and R. Jansen, Physical Review B - Condensed Matter and Materials Physics **87**, 085307 (2013).

[22] J. Y. Park, S. H. C. Baek, S. Y. Park, Y. Jo, and B. G. Park, Applied Physics Letters **107**, 182407 (2015).

[23] G. Schmidt, D. Ferrand, L. Molenkamp, A. Filip, and B. van Wees, Physical Review B - Condensed Matter and Materials Physics **62**, R4790 (2000).

[24] W. Han, X. Jiang, A. Kajdos, S. H. Yang, S. Stemmer, and S. S. P. Parkin, Nature Communications **4**, 2134 (2013).

[25] S. P. Dash, S. Sharma, J. C. Le Breton, J. Peiro, H. Jaffrès, J. M. George, A. Lemaître, and R. Jansen, Physical Review B - Condensed Matter and Materials Physics **84**, 054410 (2011).